AIMS Materials Science, 7(6): 887–901.
DOI: 10.3934/matersci.2020.6.887
Received: 29 September 2020
Accepted: 15 December 2020
Published: 21 December 2020

http://www.aimspress.com/journal/Materials

Research article

Mechanical properties and corrosion behavior of novel β-type biomaterial Zr–6Mo–4Ti–xY alloys in simulated body fluid Ringer's lactate solution for implant applications

Muhammad Awwaluddin[1,*], Djoko Hadi Prajitno[2], Wisnu Ari Adi[3], Maman Kartaman[4] and Tresna P. Soemardi[1,*]

[1] Department of Mechanical Engineering, Faculty of Engineering, Universitas Indonesia, Depok 16424, Indonesia
[2] Center for Applied Nuclear Science and Technology, National Nuclear Energy Agency of Indonesia
[3] Center for Science and Technology of Advanced Materials, National Nuclear Agency of Indonesia (BATAN), Tangerang Selatan 15314, Banten, Indonesia
[4] Center for Nuclear Fuel Technology, National Nuclear Energy Agency of Indonesia, Jakarta, 12710 Indonesia

* **Correspondence:** Email: muhammad.awwaluddin91@ui.ac.id; tsoemardi@eng.ui.ac.id.

Abstract: To develop new biomaterials for implant applications, the novel biomaterial multi component Zr–Mo–Ti–xY (x = 1, 2, 3) alloys were developed as a solution to increase mechanical properties and a corrosion resistance and to reduce the toxicity of biomaterials for implant. This research is aimed to investigate the effects of yttrium (Y) element addition to the microstructural transformation, mechanical properties and corrosion behavior of the alloy. The Zr–6Mo–4Ti–xY (x = 1, 2, 3) alloys are made by melting the metals using a vacuum single arc melting furnace with high purity argon gas flow at atmospheric pressure and tungsten electrodes with a six-times remelted process. The hardness test was conducted using the Vickers hardness tester, the microstructure analysis was done using the optical microscopes, and the alloy compound and phases using the XRD and corrosion resistance test were carried out using the polarization method in simulated body fluid Ringer's lactate solution. The values of the hardness test of Zr–6Mo–4Ti–xY (x = 1, 2, 3) alloys are 461.8, 301.5 and 335.1 HV, respectively. The basketweave-shaped microstructure with the addition of yttrium moderately creates little grain measure. The corrosion rate of Zr–6Mo–4Ti–xY (x = 1, 2, 3) alloys which

are 0.3159, 0.2705 and 0.3759 mpy respectively, are categorized as outstanding (the corrosion resistance of <1 mpy) so that it can be considered as a potential biomaterial for implant applications.

Keywords: Zr alloy; corrosion resistance; yttrium; biomaterial; Zr–6Mo–4Ti–xY

1. Introduction

Biomaterials are materials that can be used as implants or a medical device and made to replace the structure and function of biological parts [1,2]. Zr–Mo–Ti is one of the candidate biomaterials to replace the hard tissue of the human body, however the corrosion materials are yet to analyze [3]. Zr has several advantages including excellent corrosion resistance [4–8] and satisfactory biocompatibility properties [9,10]. In beta phase (β-Zr) Zr has a low modulus of elasticity [11] making this material can be developed as a biomaterial. Besides that, Zr alloy has lower magnetic properties than Ti alloys, Co–Cr alloys, and stainless steels when exposed to magnetic fields from MRI devices [7,12–14].

The main problem with biomaterials is corrosion which causes toxins in the body [15–19]. In this case, corrosion resistance is important to conduct since it is a prominent factor in the biocompatibility of implants in the functioning of body tissues [15]. One way to increase corrosion resistance in an implant material is to add another metal in the alloy that can stabilize the beta phase (β-Zr), one of them is yttrium [20]. In the previous study conducted by Huang et al. [21], yttrium was proven to be able to increase corrosion resistance in Zr–Al–Cu–Ni alloys [21]. The addition of yttrium to Zr alloy can also reduce porosity, high density, and high bending strength, increase compressive strength and are suitable for biomedical applications [22]. This research is aimed to develop potential biomaterial for implant applications. The Zr–6Mo–4Ti–xY alloys are designed by using 1, 2, 3 wt% yttrium. Compound and phase composition, microstructure, mechanical properties (hardness), and corrosion resistance have been analyzed.

2. Materials and methods

The alloy compositions, Zr–6Mo–4Ti–xY (x = 1, 2, 3), were melted by using arc melting furnace of the mixture of pure zirconium (Zr, Aldrich) with 99.9 wt% purity, Mo with 99.8 wt% purity, Ti (titanium) with 99.9 wt% purity and Y (yttrium) chips ESPI metals with (99.9 wt%) purity. The ingot was remelted six times in order to obtain a homogeneous composition. Ingots with diameter of 20 mm and width 6 mm were fabricated by copper mold casting method under high-purity argon atmosphere.

In terms of corrosion testing, the ASTM standard G59-94 was referred as the standard whereas the specimens were cathodically and anodically polarized in Ringer's lactate solution at room temperature (24.2 ºC) with humidity 57% RH. The testing employed three electrode cell configurations consisting of working electrode specimens, platinum electrode, and saturated calomel electrode (SCE). The specimens of Zr–6Mo–4Ti–xY (x = 1, 2, 3) in which each has been tested three times was the working electrode. The counter electrode was platinum wire and the reference electrode was calomel (SCE). The corrosion rate measurements were performed with a Gamry Instrument Reference 600 and analysed with Gamry E-Chem software so that the I_{corr} and corrosion

rate (mpy) value are obtained. The potentiodynamic polarization curves were recorded between start potential of −1 E_{OCP} and stop potential of 1 E_{OCP} with potential sweep scan rate of 10 mV/s and step 1 mV in anodic direction after monitoring the open circuit potential (OCP) for 10 min. The potentiodynamic testing was done by scanning the voltage from −1 volt of Eocp to +1 volt of Eocp. When the sample is polarized at this voltage interval, it will produce an electric current due to the potential differences applied to the samples. The changes of current during the potentiodynamic testing process were then plotted on a voltage vs current graph (current log). The corrosion rate was measured by using the tafel extrapolation technique in the Gamry Echem DC 105 software through three steps. First, the linear regions on the anodic and cathodic curves were selected. After selecting the anodic and cathodic areas, the curve of the fitting results can be obtained by selecting the tafel fit menu in the DC 105 software. Tafel analysis was done by extrapolating the linear portion of the log plot current versus potential at the junction of anodic and cathodic current in which the extents were intersected. This intersection obtained the corrosion current density (I_{corr}). Corrosion parameters obtained by this tafel fit method are I_{corr}, E_{corr}, βa, and βc. We calculated the corrosion rate using the following equation (Eq 1):

$$CR = K\frac{ai}{nD} \tag{1}$$

where *CR* is the corrosion rate in mils per years (mpy); *K* is the constant factor, for unit mpy is 0.129; *D* is the density in g/cm^3; *a* is the atomic weight of metal; *i* is the current density (μA/ cm^2); *n* is the number of electron lost.

The electrochemical impedance spectroscopy (EIS) was obtained by using the potentiostat G300 potentiostat/galvanostat Gamry series connected to the DC 105 software. Acquisition data was obtained by EIS300 software. The data were acquired by the polarization of the working electrode from 100 KHz to 10 Hz with AC current 0.1 mA.

The chemical compositions of human body fluids simulation were shown in Table 1. Sodium chloride (NaCl) was the dominant composition. The chloride ions are the cause of corrosion biomaterials, including Zr–6Mo–4Ti–xY (x = 1, 2, 3), so these fluids are suitable for analyzing the corrosion resistance.

Table 1. Chemical compositions of human body fluids simulation.

Reagent	Composition
Calcium chloride dihydrate ($CaCl_2{\cdot}2H_2O$)	0.10 g
Potassium chloride (KCl)	0.15 g
Sodium chloride (NaCl)	3.00 g
Sodium (Na)	130 mEq/L
Potassium (K)	4 mEq/L
Calcium (Ca)	2.7 mEq/L
Sodium lactate	1.55 g
Water for injection	500 mL
Chloride	108.7 mEq/L
Lactate (HCO_3^-)	28 mEq/L
Osmolarity	273 mOsm/L

3. Results and discussion

In this research, we focus on the mechanical properties and good corrosion resistance to reduce toxicity in the human body. The chemical composition of Zr–6Mo–4Ti–xY (x = 1, 2, 3) alloys used in this research are displayed in Table 2. The amount of the elements used (wt% as the unit) are indicated from the number attached to each element. The Zr is the balancing element in which it changes in response to the change of the amount of Y used. In this research, the amount of yttrium acts as the variable factor.

Table 2. The chemical composition of Zr–6Mo–4Ti–xY.

Composition alloy (as cast)	Zr		Mo		Ti		Y	
	wt%	g	wt%	g	wt%	g	wt%	g
Zr–6Mo–4Ti–1Y	89	13.35	6	0.9	4	0.6	1	0.15
Zr–6Mo–4Ti–2Y	88	13.20	6	0.9	4	0.6	2	0.30
Zr–6Mo–4Ti–3Y	87	13.05	6	0.9	4	0.6	3	0.45

The XRD patterns of the biomaterial Zr–6Mo–4Ti–xY (x = 1, 2, 3) alloys are displayed in Figure 1, where the profile of the quaternary shows the existence of β phases of zirconium. From Figure 1, it can be seen that the β-phase alloy with bcc crystal structure in the plane orientations of 110, 200, 211 for the Zr–6Mo–4Ti–xY (x = 1, 2, 3) alloys respectively, lies at the diffraction angle of Bragg on 41.11°, 60.21°, 75.43°; 41.75°, 60.45°, 75.57° and 41.83°, 60.55°, 75.87°. It appears that there is a shift to the right of the Bragg diffraction peak as the element fraction Y increases. These results show that the substitution effect of the Y atom in the Zr–6Mo–4Ti alloy has been successfully carried out. The right shifting indicates that d lattice expansion occurs because the Y atom has a larger atomic radius (rY = 180 pm) than the atomic radius of Zr (rZr = 155 pm), Mo (rMo = 145 pm) and Ti (rTi = 140 pm). The results of d lattice expansion are incurred in the unit cell volume.

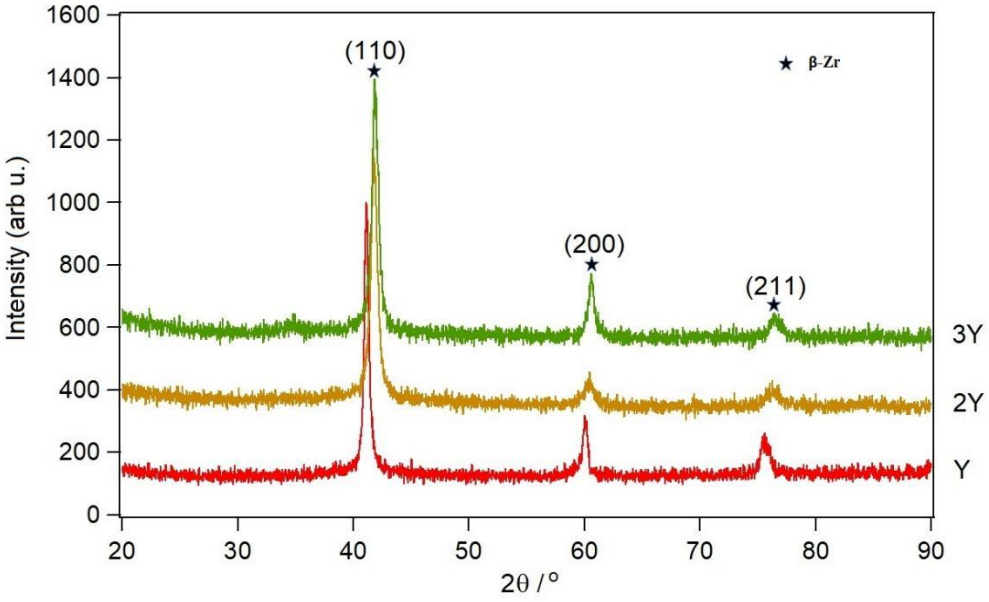

Figure 1. Diffraction patterns of the Zr–6Mo–4Ti–xY (x = 1, 2, 3) alloys.

Table 3 shows the analysis results of the variation of lattice constant, unit cell volume and alloy density of Zr–6Mo–4Ti–xY (x = 1, 2, 3) using GSAS software. β-Zr has a cubic structure with a space group of 1–3 m. There are two Zr atoms occupying the 2a Wyckoff site (0, 0, 0) of each unit cell [23]. When compared with β-Zr, it is known that the lattice constants and the unit cell volume of Zr–6Mo–4Ti–xY (x = 1, 2, 3) appear to be lower than the lattice constants unit cell volume β-Zr. This is because the dominant substitutions of β-Zr are Mo and Ti which have a lower atomic radius than Zr. Whereas the presence of the substitution of Y into the alloy can increase the lattice constant and volume of the unit cell because Y has a larger atomic radius than Zr. Thus, as the Y content increases, the lattice constant and volume of the unit cell become bigger and closer to β-Zr. Based on Table 3, it was also found that the atomic density of the Zr–6Mo–4Ti–xY (x = 1, 2, 3) alloys was greater than that of β-Zr. The greater the Y content, the greater the atomic density of the Zr–6Mo–4Ti–xY (x = 1, 2, 3) alloys. The largest contribution to the atomic density of the Zr–6Mo–4Ti–xY alloy is the Mo atom (10.282 gr/cm^3). While the atomic density of Y is 4.472 gr/cm^3 as a counterweight to density of Ti (3.076 gr/cm^3) which is relatively low compared to the Zr atom (6.386 gr/cm^3). In consequence, it can be concluded that the enhancement of Y content in Zr–6Mo–4Ti alloys cannot make them lighter.

Table 3. Parameter of lattice constants, unit cell volume and alloys density of Zr–6Mo–4Ti–xY (x = 1, 2, 3).

Alloys	α (Å)	v (Å^3)	p (g/cm^3)	Reference
Zr–6Mo–4Ti–1Y	3.5496	44.72	7.973	This work
Zr–6Mo–4Ti–2Y	3.5610	45.15	8.473	This work
Zr–6Mo–4Ti–3Y	3.5550	44.95	8.769	This work
Zr	3.5680	45.42	6.670	[23]

The optical microscope images of the microstructures of β-type Zr–6Mo–4Ti–xY (x = 1, 2, 3) alloys synthesized from a six-cycle melting process are displayed in Figure 2. Due to the solubility of alloying elements in Zr, the equiaxed β crystal grain can be clearly observed. The grain boundaries which form the large grains of β phase are definitely seen. The grain size length of β-type Zr–6Mo–4Ti–xY (x = 1, 2, 3) alloys is 100–326 μm. It was observed that the grain of β-Zr became smaller and the microstructure was refined with the increase of Y content.

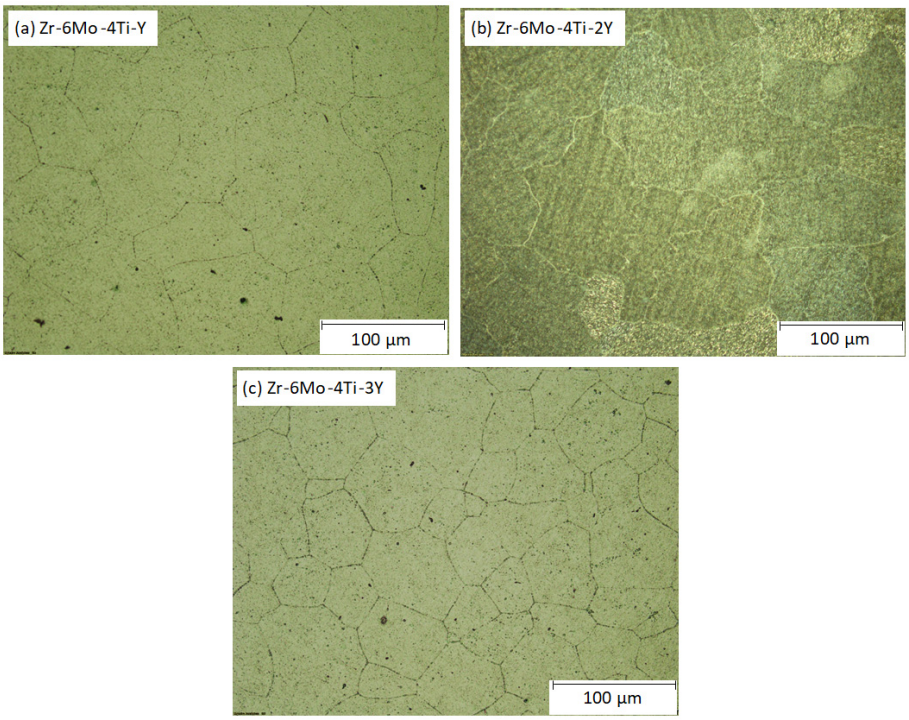

Figure 2. Optical microscope images of the as-cast of the β-type Zr–6Mo–4Ti–xY (x = 1, 2, 3) biomedical alloys.

The plot of the Vickers' microhardness values of the β-type Zr–6Mo–4Ti–xY (x = 1, 2, 3) biomedical alloys are displayed in Table 4. It can be observed that the addition of Y changes the hardness values of the β-type Zr–6Mo–4Ti–xY (x = 1, 2, 3) biomedical alloys. The hardness value of Zr–6Mo–4Ti–Y was 461.8 HV, which then decrease to 335.1 HV after the addition of 2 wt% Y. This decrease was resulted from the changes in the grain size of β-phase Zr–6Mo–4Ti–2Y biomedical alloys. In addition to 3 wt% Y, the hardness value is 301.5 HV. Therefore, it can be concluded that the addition of 3 wt% Y in Zr–6Mo–4Ti alloys make them soft.

Table 4. Vicker's hardness values of the β-type Zr–6Mo–4Ti–xY (x = 1, 2, 3) according to addition of Y content.

Sample (alloy)	HV				
	1	2	3	4	Average
Zr–6Mo–4Ti–1Y	466	482	465	434	461.8
Zr–6Mo–4Ti–2Y	343	331	316	350	335.1
Zr–6Mo–4Ti–3Y	304	302	303	297	301.5

The hardness values of the Zr–6Mo–4Ti–2Y alloy decreased when added 1 wt% Y from the Zr–6Mo–4Ti–Y alloy due to an increase in the grain size of β-phase in Zr–6Mo–4Ti–2Y alloy, as shown in Figure 2b. The grain growth in the β-phase Zr gets better as the Y content increases to 3 wt% leading to a slight decrease in the hardness value of the Zr–6Mo–4Ti–3Y alloy as shown in Figure 2c. It can be concluded that the phase and grain size can affect the hardness values of Zr–6Mo–4Ti–xY (x = 1, 2, 3) biomaterial alloys.

The polarization curves of the corrosion test results of the Zr–6Mo–4Ti–xY (x = 1, 2, 3) alloys in Ringer's lactate solution simulating human body fluid are displayed in Figure 3. The corrosion rate is generally determined by the equilibrium between opposing electrochemical reactions, namely anodic reactions, in which the metal is oxidized by removing electrons from the metal, then a cathodic reaction in which a solution containing O_2^- or H^+ is able to reduce electrons in the metal. When these two reactions are in equilibrium, no electron flow occurs. Figure 3 shows that the vertical axis is the electric potential and the horizontal axis is the logarithm of the absolute current. Theoretically, the currents for anodic and cathodic reactions are represented as a straight line. The curved line is the total current which is the sum of the anodic current and the cathodic current. A sharp line in the curve is the point where the current reverses polarity as the reaction changes from anodic to cathodic, or vice versa. In this case the metal acts to maintain a balance of the anodic and cathodic reactions. If an anodic reaction removes too many electrons from the metal, the excess electrons can shift the metal potential towards a more negative direction, which means slowing down the anodic reaction and accelerating the cathodic reaction.

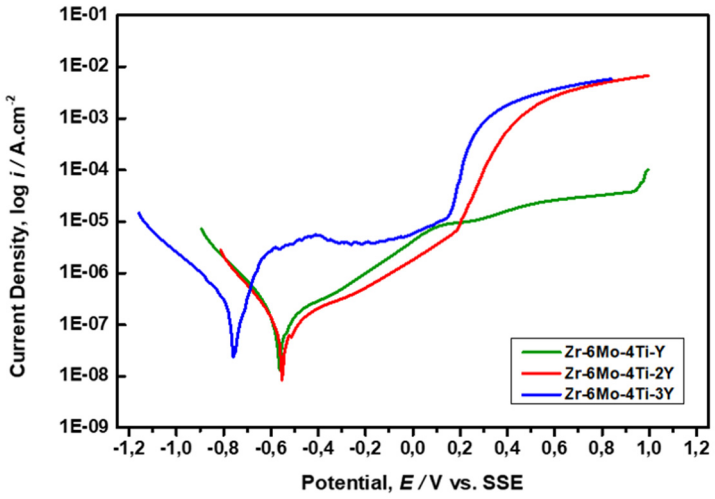

Figure 3. Potentiodynamic polarization curve of Zr–6Mo–4Ti–xY (x = 1, 2, 3) in Ringer's lactate solution.

According to the results of research conducted by Lee and Liu [24,25], it shows that the addition of Y can increase the corrosion resistance of the alloy as long as Y can be completely dissolved in the alloy. Meanwhile, if Y is not completely dissolved in the alloy, the Y network structure will be oriented towards the grain boundaries and very easily bind with oxygen to form Y_2O_3. However, based on the morphological observations of the alloy particles Zr–6Mo–4Ti–xY (x = 1, 2, 3) in Figure 2 it was found that the sample appeared to have very good homogeneity so that it was assumed that Y was completely dissolved in the alloy. This is supported by the XRD analysis data in Figure 1 in which the alloy has a single phase to form a solid solution of the b-Zr structure. While the results of the corrosion analysis show that the alloy with the addition of Y at the composition x = 3, the corrosion rate of the alloy increases again. This condition indicates an anomaly which can be explained based on understanding the crystal structure of the material. The X-ray diffraction pattern of alloys with a concentration of x = 1 and x = 3 appears to undergo crystallographic plane

orientation in the direction (200), while the X-ray diffraction pattern of alloys with a concentration of x = 2 does not. It is possible that the crystal orientation of a certain plane in this alloy occurs during the melting process. The presence of this crystal orientation will result in crystal defects in the alloy, so that this position is thought to be very prone to corrosion. Therefore, the corrosion rate of the alloy at a concentration of x = 1 and x = 3 increases.

The potentiodynamic curve of all variation composition of Zr–6Mo–4Ti–xY (x = 1, 2, 3) synthesized involves a six-cycle melting process. The curves included cathodic and anodic behavior. Potentiodynamic polarization tests were carried out from −1000 mV to +2000 mV versus Open Circuit Potential (E_{ocp}) for all alloys. If the setpoint potential is continuously increased (above E_{ocp}), an anodic polarization curve is generated. Conversely, if the potential is continuously decreased (below E_{ocp}), a cathodic polarization curve is produced. Based on Figure 3, at the potential under E_{ocp}, which is from −1000 mV to E_{ocp}, reduction reaction occurs that indicate with decreasing current density, while the potential above E_{ocp} until +2000 mV, oxidation reaction occurred that indicate with increasing of current density. Over potential was applied from the most negative value to the positive and then current density measurement started. The scan kept moving and reached corrosion potential (E_{corr}) and corrosion current density (i_{corr}). Each alloy will have a specific value of E_{corr} and i_{corr}. The corrosion current represents the degree of degradation of the alloy and is used to determine the corrosion rate of the alloy. The alloy that has the most positive value of E_{corr} means that the corrosion is difficult to occur thermodynamically while as for i_{corr}, a less value of i_{corr} indicates low corrosion rate. It can be seen the effect of increasing the amount of Y into the Zr–6Mo–4Ti alloy has shifted the E_{corr} to more negative value, which means the corrosion is getting easier to occur. Corrosion current density was calculated using tafel extrapolation as Figures 4–6. After that corrosion rates were calculated according to ASTM Standard G102. Tafel analysis is done by extrapolating the linear portion of the log plot current versus potential at the junction of anodic and cathodic current. This method requires the presence of a linear or Tafel section in the E versus log I curve. E_{corr} potential scan of approximately 250 mV is generally required to determine the linear section of at least one-decade current as presented. A reasonably accurate extrapolation can be made to the E_{corr} potential.

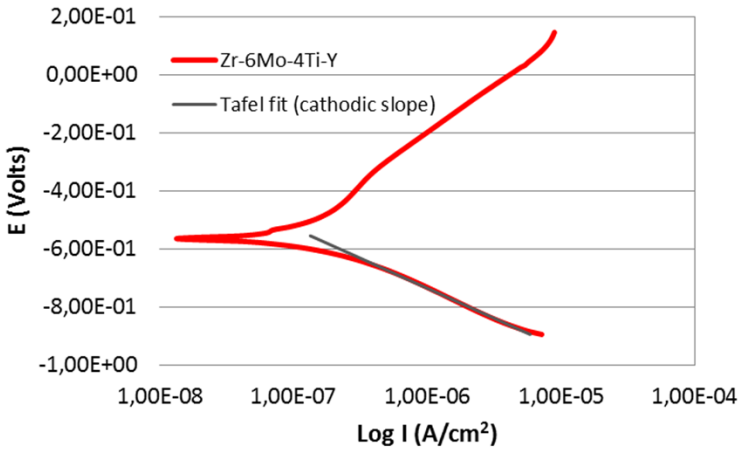

Figure 4. Tafel fit analysis to determine the corrosion current density of Zr–6Mo–4Ti–Y alloy.

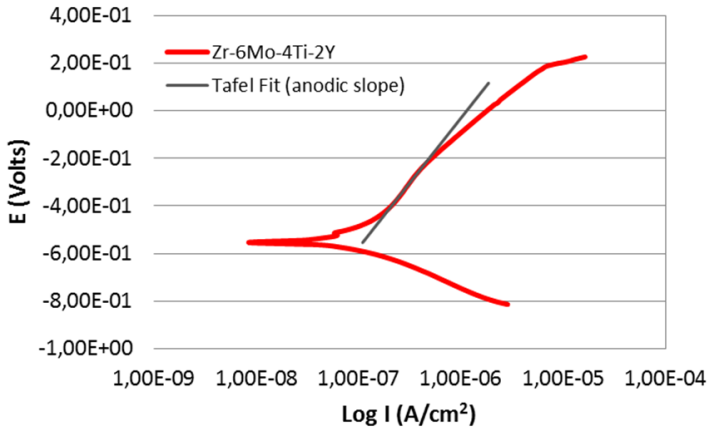

Figure 5. Tafel fit analysis to determine the corrosion current density of Zr–6Mo–4Ti–2Y alloy.

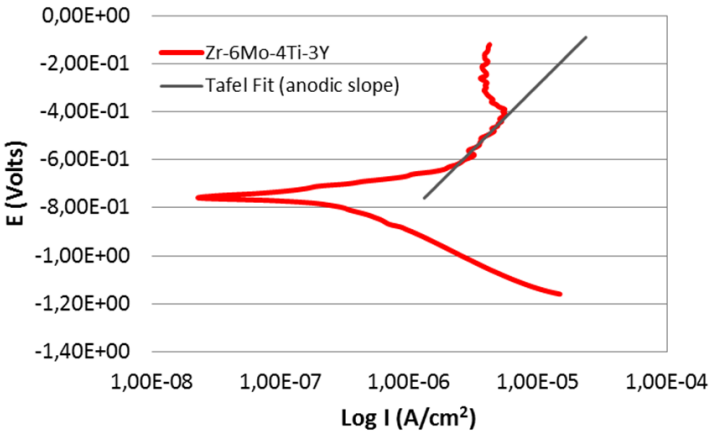

Figure 6. Tafel fit analysis to determine the corrosion current density of Zr–6Mo–4Ti–3Y alloy.

The electrochemical parameters, corrosion potential (E_{corr}) and corrosion current density (i_{corr}) of Zr–6Mo–4Ti–xY (x = 1, 2, 3) alloys in Ringer's lactate solution, are displayed in Table 5. The corrosion rates of Zr–6Mo–4Ti–xY (x = 1, 2, 3) are 0.3159, 0.2705 and 0.3759 mpy, respectively. The additions of Y element in alloys from 1 to 3 wt% tend to increase the corrosion rate of the alloys, although the alloy with 2 wt% Y has the lowest corrosion rate. The Increase of the corrosion potential indicates that the oxide layer on the surface was more stable. The corrosion rate difference may be caused by the grain size changes and the presence of β-phase. Apart of the lowest corrosion rate of the Zr–6Mo–4Ti–2Y alloy, The potentiodynamic corrosion test data shown in Table 5 provide an evidence that the Zr–6Mo–4Ti–xY (x = 1, 2, 3) alloys have the average better corrosion resistance than the commercial biomaterial Ti–6Al–4V (5.04 mpy) and other Ti alloys like Ti–6Mo–6Nb–4Sn–4Mn (9.72 mpy), Ti–6Mo–6Nb–4Sn–8Mn (1.98 mpy), Ti–6Mo–6Nb–8Sn–4Mn (1.60 mpy), and Ti–6Mo–6Nb–8Sn–8Mn (1.63 mpy) [26].

Table 5. Corrosion parameters of the Zr–6Mo–4Ti–xY (x = 1, 2, 3) alloy in Ringer's lactate solution.

Alloy	Beta A (V/decade)	Beta C (V/decade)	E_{corr} (V)	I_{corr} (A)	CR (mpy)
Zr–6Mo–4Ti–1Y	0.5665	0.1987	−0.567	1.75×10^{-7}	0.3159
Zr–6Mo–4Ti–2Y	0.7727	0.2112	−0.556	1.49×10^{-7}	0.2705
Zr–6Mo–4Ti–3Y	0.1398	0.2231	−0.754	2.08×10^{-7}	0.3759

Electrochemical impedance spectroscopy is one of the power full tool and widely used experimental in electrochemistry. The application of EIS ranging from corrosion, energy storage and power generation. Considering the broad applicability of the EIS technique, it is critical to validate the EIS data against the Kramers–Kronig relations. Kramers–Kronig proposed several scores that provide quick methods for the evaluation of the EIS data quality. The Electrochemical Impedance Spectroscopy (EIS) study of Zr-base Zr–6Mo–4Ti–xY (x = 1, 2, 3) alloys were performed in Ringer's lactate solution in order to evaluate interface electrochemical behavior and physical process at the electrode electrolyte interface between Zr-base alloys with Ringer's lactate.

Figure 7 depicted the Bode plot data Zmod impedance as vertical axis and frequency as horizontal axis and Kramers–Kronig (K–K) relation that showed plot data residual Zmod real as vertical axis and frequency as horizontal axis. The Kramers–Kronig Relations consist of a set of transformation which can be used to predict one component of impedance over entire the frequency from zero to unlimited for electrochemical impedance spectroscopy (EIS) data. The EIS data is satisfied or not can be check by K–K relation for fitting [27]. By EIS 300 software the data EIS can be fitting and the result as shown in Table 6. Figure 7a,c,e depicted that Bode data plot of the Zr–6Mo–4Ti–xY (x = 1, 2, 3) alloys with the data fitting by Kramers–Kronig analysis as implemented by the Gamry software. These results show good simulations yielded goodness of fit correlation at low to high frequency as seen in Figure 7a,c,e.

The residual errors for a complex fit to Kramers–Kronig analysis as implemented by the Gamry software for low to high frequency are presented in Figure 7b,d,f. These results simulations yielded goodness of fit at low to high frequency as seen in Table 6. The Kramers–Kronig relations showed these simulated data to be consistent of the impedance yielded a semicircle.

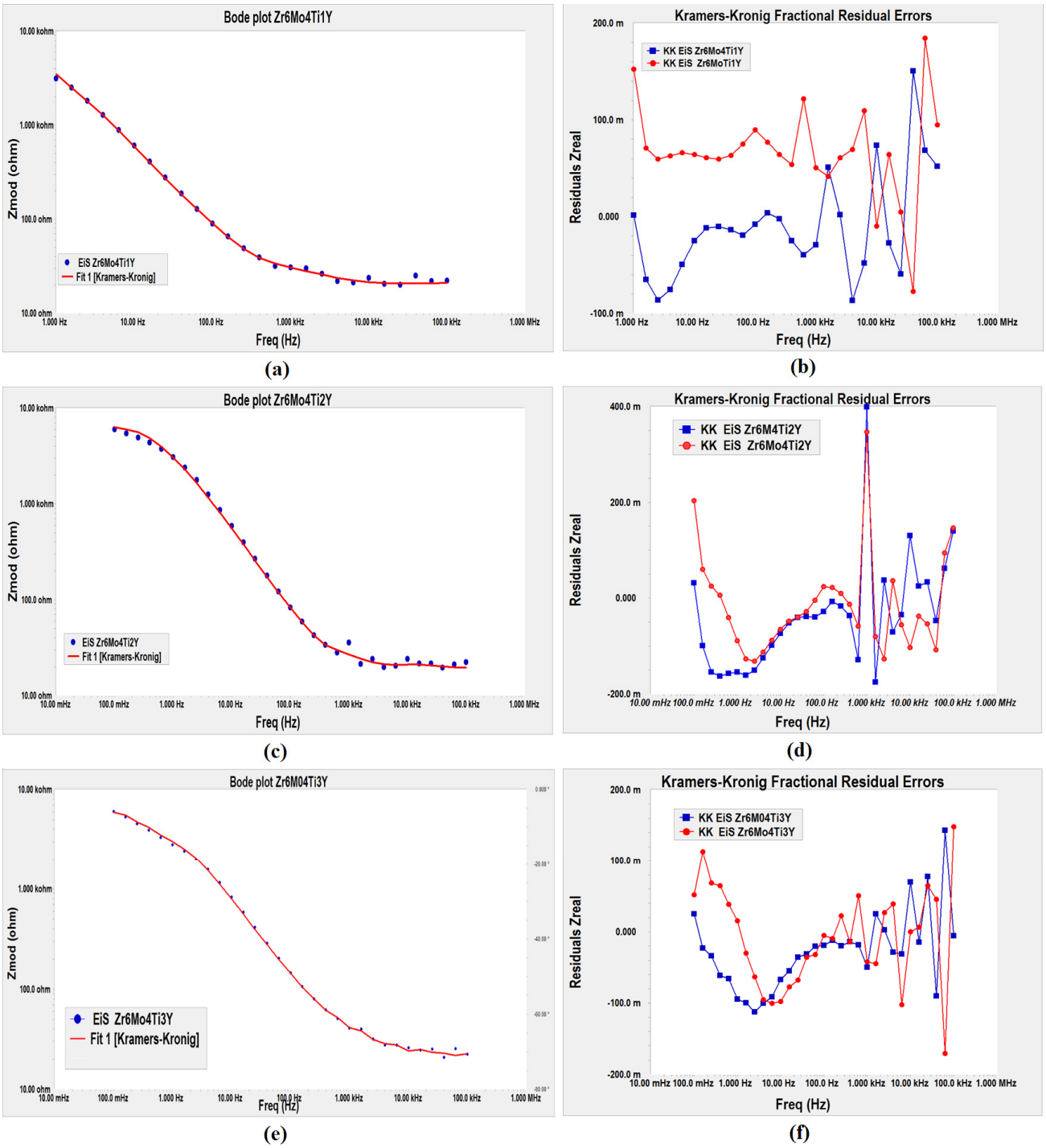

Figure 7. Bode plot and Kramers–Kronig fractional residual errors curve. (a) Bode plot curve for Zr6Mo4TiY alloy; (b) Kramers–Kronig residual errors curve for Zr6Mo4TiY alloy; (c) Bode plot curve for Zr6Mo4Ti2Y alloy; (d) Kramers–Kronig residual errors curve for Zr6Mo4Ti2Y alloy; (e) Bode plot curve for Zr6Mo4Ti3Y alloy; (f) Kramers–Kronig residual errors curve for Zr6Mo4Ti3Y alloy.

Table 6. The data parameter goodness of fit Zr–6Mo–4Ti–xY (x = 1, 2, 3).

Parameter	File name	Value
Goodness of fit	Galvano EIS Zr6Mo4TiY	8.603×10^{-3}
	Galvano EIS Zr6Mo4Ti2Y	20.82×10^{-3}
	Galvano EIS Zr6Mo4Ti3Y	6.190×10^{-3}

Figure 8 depicted the Nyquist plot data of three different Zr-base alloys in Ringer's lactate solution in which the real impedance data are plotted on the horizontal axis and the imaginary impedance data are plotted on the vertical axis. The Nyquist graph is a relationship between the real impedance against imaginary impedance with graph shaped semi-circle. The characteristics of the Nyquist graphs for the Zr-base alloys, Zr–6Mo–4Ti–xY (x = 1, 2, 3), in Ringer's lactate are changed as the diameters of semi-circle responds to and are enlarged in line with the increase of the 2% yttrium content on the Zr-base alloys in the Ringer's lactate. Then the diameters of semi circle Nyquist plot are decrease if the Zr base alloy contain 3Y. This is evident that addition of 2 Y on the Zr–6Mo–Ti base alloy improved corrosion of the alloys as seen in Table 6 corrosion rate data from Tafel polarization. It showed that the all Nyquist plots presented the character of single capacitive loop.

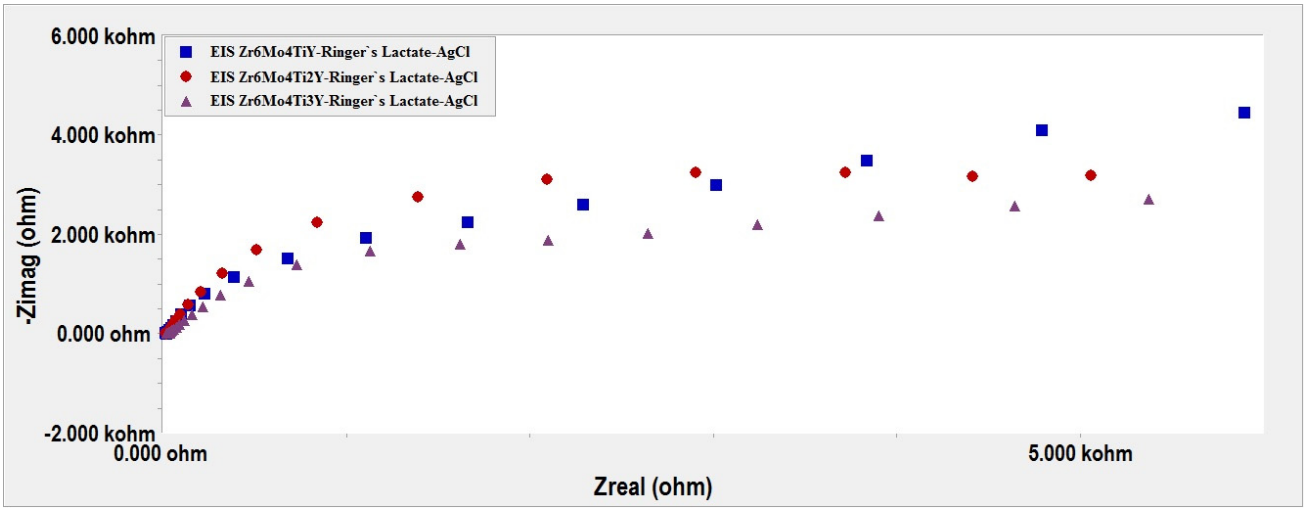

Figure 8. The Nyquist data plot for Zr–6Mo–4Ti–xY (x = 1, 2, 3), alloys in Ringer's lactate solution.

The Nyquist data plot compared with fit Kramers–Kronig can be seen at Figure 9. Figure 9 showed that Nyquist data plot of the three alloys with the data fitting by Kramers–Kronig analysis were implemented by the Gamry software. These results show good trend simulations yielded goodness of fit correlation at low to high Zreal as seen in Figure 9 and Table 6.

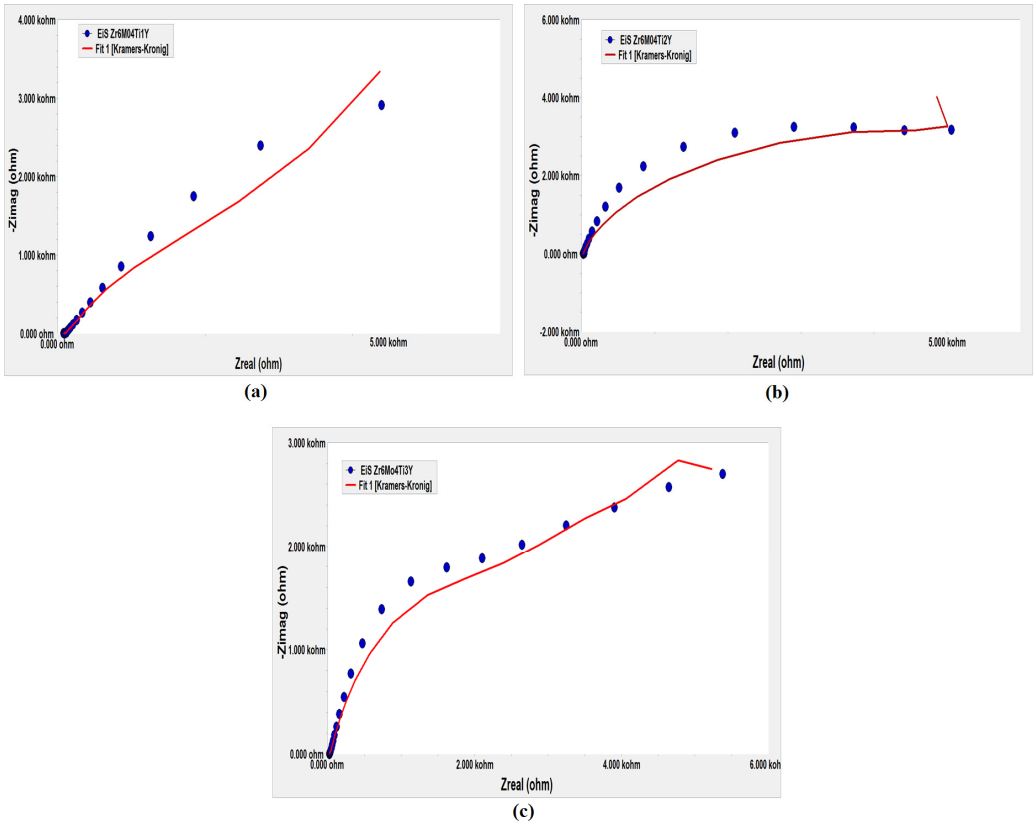

Figure 9. The Nyquist data plot compared with fit Kramers–Kronig curve. (a) The curve comparation for Zr6Mo4TiY alloy data; (b) The curve comparation for Zr6Mo4Ti2Y alloy data; (c) The curve comparation for Zr6Mo4Ti3Y alloy data.

For this research, equivalent circuit for modelling impedance data at ambient temperature which can be seen at Figure 10. Re is the reference electrode, Rs is the resistance of the solution between the working electrode and reference electrode, Cdl is the currents at the double layer capacitance, Rct or Rp is the charge-transfer resistance against corrosion.

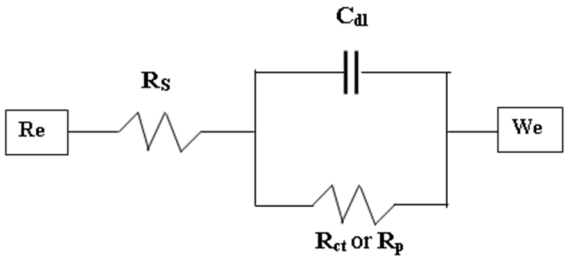

Figure 10. Equivalent circuit models used in EIS fitting data.

4. Conclusions

New biomaterials with high corrosion resistance have been developed. The β-type Zr–6Mo–4Ti–xY (x = 1, 2, 3) biomedical alloys were characterized and analyzed for the first time.

The effect of the yttrium element was investigated in the mechanical properties and in the corrosion resistance of Zr–6Mo–4Ti–xY (x = 1, 2, 3) alloys. The results are summed up as follows:

(1) The Y addition had a positive impact on the formation of β-phase zirconium in the Zr–6Mo–4Ti–xY (x = 1, 2, 3) alloys. All the casts of Zr–6Mo–4Ti–xY (x = 1, 2, 3) samples primarily contain continuous and equiaxed β-Zr phases.
(2) The mechanical properties of the Zr–6Mo–4Ti–xY (x = 1, 2, 3) have been analyzed. It is found that these alloys have the hardness value of 461.8 HV, 301.5 HV, and 335.1 HV, respectively.
(3) Finally, the corrosion resistance of the Zr–6Mo–4Ti–xY (x = 1, 2, 3) have been analyzed. The optimum corrosion rate of these alloys achieved upon the addition of 2 wt% Y is 0.2705 mpy in which it makes the alloy become potential biomedical materials for implant applications. To ensure the biocompatibility of these alloys, further studies should be conducted to determine the optimum of Y content.

Acknowledgments

This research was financially supported by PUTI Doktor grant funds with the contract number NKB-657/UN2.RST/HKP.05.00/2020. We would like to thank Yatno DS, Amd., Slamet Pribadi, Dienne, Agus Sujatno, Ganissa K.S., MT., and all engineering laboratory staff of Center for Science and Technology of Advanced Materials (PSTBM) and Center for Nuclear Fuel Technology (PTBBN) of National Nuclear Energy Agency of Indonesia (BATAN) for the material testing.

Conflicts of interests

All authors declare no conflicts of interest in this paper.

References

1. Poitout DG (2004) *Biomechanics and Biomaterials in Orthopedics*, London: Springer.
2. Saini M, Singh Y, Arora P, et al. (2015) Implant biomaterials: A comprehensive review. *World J Clin Cases* 3: 52.
3. Nie L, Zhan Y, Liu H, et al. (2014) Novel β-type Zr–Mo–Ti alloys for biological hard tissue replacements. *Mater Des* 53: 8–12.
4. He W, Chen X, Liu N, et al. (2017) Cryo-rolling enhanced inhomogeneous deformation and recrystallization grain growth of a zirconium alloy. *J Alloys Compd* 699: 160–169.
5. Zinkle SJ, Was G (2013) Materials challenges in nuclear energy. *Acta Mater* 61: 735–758.
6. Chen L, Li J, Zhang Y, et al. (2016) Effect of low-temperature pre-deformation on precipitation behavior and microstructure of a Zr–Sn–Nb–Fe–Cu–O alloy during fabrication. *J Nucl Sci Technol* 53: 496–507.
7. Chen Q, Thouas GA (2015) Metallic implant biomaterials. *Mat Sci Eng R* 87: 1–57.
8. Narushima T (2019) New-generation metallic biomaterials, In: Niinomi M, *Metals for Biomedical Devices*, 2 Eds., Cambridge: Woodhead Publishing, 495–521.
9. Pratama NR, Faizal F, Prajitno DH (2020) Corrosion behavior of ternary Zr–25Ti–5Sn alloy doped with Ge as biomaterials implant in simulation body fluid solution. *IJMEA* 1: 59–67.

10. Moztarzadeh A (2017) Biocompatibility of implantable materials focused on titanium dental implants. [PhD's thesis]. Charles University, Prague.
11. Xia CQ, Jiang XJ, Wang XY, et al. (2015) Microstructure and mechanical properties of hot-rolled ZrB alloys. *Mat Sci Eng A-Struct* 628: 168–175.
12. Nomura N, Oya K, Tanaka Y, et al. (2010) Microstructure and magnetic susceptibility of as-cast Zr–Mo alloys. *Acta Biomater* 6: 1033–1038.
13. Shafiei F, Honda E, Takahashi H, et al. (2003) Artifacts from dental casting alloys in magnetic resonance imaging. *J Dent Res* 82: 602–606.
14. Nomura N, Tanaka Y, Kondo R, et al. (2009) Effects of phase constitution of Zr–Nb alloys on their magnetic susceptibilities. *Mater Trans* 50: 2466–2472.
15. Eliaz N (2019) Corrosion of metallic biomaterials: A review. *Materials* 12: 407.
16. Chelariu R, Trinca LC, Munteanu C, et al. (2017) Corrosion behavior of new quaternary ZrNbTiAl alloys in simulated physiological solution using electrochemical techniques and surface analysis methods. *Electrochim Acta* 248: 368–375.
17. Akimoto T, Ueno T, Tsutsumi Y, et al. (2018) Evaluation of corrosion resistance of implant-use Ti–Zr binary alloys with a range of compositions. *J Biomed Mater Res* 106: 73–79.
18. Yu L, Tang J, Qiao J, et al. (2017) Effect of yttrium addition on corrosion resistance of Zr-based bulk metallic glasses in NaCl solution. *Int J Electrochem Sci* 12: 6506–6519.
19. Zhou FY, Wang BL, Qiu KJ, et al. (2012) Microstructure, corrosion behavior and cytotoxicity of Zr–Nb alloys for biomedical application. *Mat Sci Eng C-Bio S* 32: 851–857.
20. Wang ZM, Ma YT, Zhang J, et al. (2008) Influence of yttrium as a minority alloying element on the corrosion behavior in Fe-based bulk metallic glasses. *Electrochim Acta* 54: 261–269.
21. Huang L, Qiao D, Green BA, et al. (2009) Bio-corrosion study on zirconium-based bulk-metallic glasses. *Intermetallics* 17: 195–199.
22. Chiapasco M, Casentini P, Zaniboni M, et al. (2012) Titanium–zirconium alloy narrow-diameter implants (S traumann R oxolid®) for the rehabilitation of horizontally deficient edentulous ridges: prospective study on 18 consecutive patients. *Clin Oral Implan Res* 23: 1136–1141.
23. Kutsar A, German V, Nosova G (1973) Alpha to omega/-transformation in titanium and zirconium in shock waves. *Dokl Akad Nauk SSSR* 213: 81–84.
24. Lee L, Greene ND (1963) Corrosion characteristics of the rare earth and yttrium metals. Available from: https://www.osti.gov/servlets/purl/4712390.
25. Liu X, Shan D, Song Y, et al. (2017) Influence of yttrium element on the corrosion behaviors of Mg–Y binary magnesium alloy. *J Magnes Alloy* 5: 26–34.
26. Sutowo C, Senopati G, Pramono AW, et al. (2020) Microstructures, mechanical properties, and corrosion behavior of novel multi-component Ti–6Mo–6Nb–xSn–xMn alloys for biomedical applications. *AIMS Mater Sci* 7: 192–202.
27. Schönleber M, Klotz D, Ivers-Tiffée E (2014) A method for improving the robustness of linear Kramers–Kronig validity tests. *Electrochim Acta* 131: 20–27.

AIMS Press

© 2020 the Author(s), licensee AIMS Press. This is an open access article distributed under the terms of the Creative Commons Attribution License (http://creativecommons.org/licenses/by/4.0)